

Cycle-Consistent Bridge Diffusion Model for Accelerated MRI Reconstruction

Tao Song^{a,b,*}, Yicheng Wu^{c,*}, Minhao Hu^d, Xiangde Luo^e, Guoting Luo^f, Guotai Wang^e, Yi Guo^a, Feng Xu^a,
Shaoting Zhang^{b,**}

^a*School of Information Science and Technology, Fudan University, Shanghai, China*

^b*Shanghai AI Lab, Shanghai, China*

^c*Faculty of Information Technology, Monash University, Melbourne, Australia*

^d*University of Oxford, London, UK*

^e*School of Mechanical and Electrical Engineering, University of Electronic Science and Technology of China, Chengdu, China*

^f*Department of Radiology, Sichuan Provincial People's Hospital, Chengdu, China*

Abstract

Accelerated MRI reconstruction techniques aim to reduce examination time while maintaining high image fidelity, which is highly desirable in clinical settings for improving patient comfort and hospital efficiency. Existing deep learning methods typically reconstruct images from under-sampled data with traditional reconstruction approaches, but they still struggle to provide high-fidelity results. Diffusion models show great potential to improve fidelity of generated images in recent years. However, their inference process starting with a random Gaussian noise introduces instability into the results and usually requires thousands of sampling steps, resulting in sub-optimal reconstruction quality and low efficiency. To address these challenges, we propose Cycle-Consistent Bridge Diffusion Model (CBDM). CBDM employs two bridge diffusion models to construct a cycle-consistent diffusion process with a consistency loss, enhancing the fine-grained details of reconstructed images and reducing the number of diffusion steps. Moreover, CBDM incorporates a Contourlet Decomposition Embedding Module (CDEM) which captures multi-scale structural texture knowledge in images through frequency domain decomposition pyramids and directional filter banks to improve structural fidelity. Extensive experiments demonstrate the superiority of our model by higher reconstruction quality and fewer training iterations, achieving a new state of the art for accelerated MRI reconstruction in both fastMRI and IXI datasets.

Keywords: Accelerated MRI reconstruction, Cycle-Consistent Bridge Diffusion, Contourlet Decomposition Embedding

1. Introduction

Magnetic resonance imaging (MRI) is widely used in clinical practice since it can highlight soft tissues with diverse contrasts. However, MRI scanning is slow ((e.g.,) a 1.5T brain examination typically takes 35-45 minutes Sar-

toretti et al. (2019)), leading to high costs and more motion artifacts Zaitsev et al. (2015). Therefore, accelerated MRI reconstruction attracts great attention and various deep learning-based approaches have been proposed to reduce the scanning time and improve the reconstruction quality Hyun et al. (2018); Jeelani et al. (2018); Fabian et al. (2021).

In general, accelerated MRI reconstruction aims to exploit fast-scanned MRI sequences, that are under-sampled in the k-space, and then transform them to full-sampled high-quality MRI data. Given the physical foundation in

*Equal Contribution

**Corresponding author

Email address: Zhangshaoting@pjlab.org.cn (Shaoting Zhang)

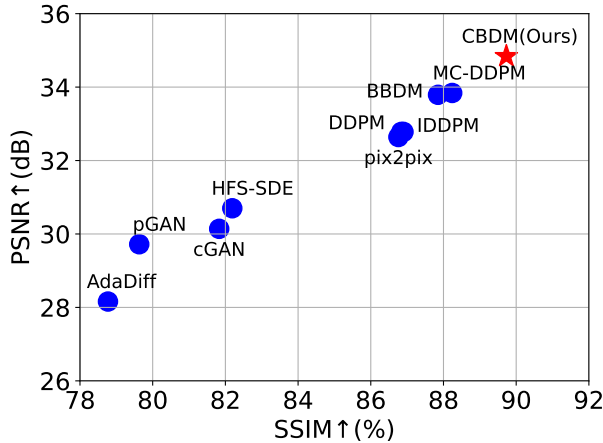


Figure 1: Comparisons with state-of-the-art methods in terms of PSNR and SSIM results on the fastMRI knee dataset.

MRI reconstruction, data-driven works are often incorporated with traditional reconstruction operations to enhance both the model interpretability and imaging process. For example, Aggarwal et al. (2018); Sun et al. (2016); Zhang and Ghanem (2018a); Cui et al. (2021); Hou and Li (2022) suggest converting the iterative optimization process used in traditional compressed sensing (CS) techniques into trainable neural network. Similarly, Sriram et al. (2020); Lv et al. (2021); Knoll et al. (2020) integrate traditional parallel imaging methods into deep neural networks to improve performance. Generative Adversarial Networks (GANs) Goodfellow et al. (2014) are also proposed to facilitate MRI reconstruction, boosting the generation performance Huo et al. (2018); Lv et al. (2021); Yang et al. (2021); Cole et al. (2020). For instance, Chen et al. (2021) enhanced the discriminative ability of GANs using wavelet transforms to improve MRI reconstruction accuracy. Cole et al. (2020) implemented an unsupervised MRI reconstruction using GANs. Diffusion models are further used to accelerate MRI reconstruction, improving image fidelity. Xie and Li (2022); Cao et al. (2024); Hou et al. (2023) developed diffusion models incorporating measurement and high-frequency priors, reducing unnecessary diffusion regions to enhance the generation quality.

Existing methods typically require multi-coil complex-

valued data for accelerated MRI reconstruction, which is intermediate data processed within MRI scanners and thus is impractical to obtain in practice. In contrast, MRI magnitude images can be easily collected Wang et al. (2016), and magnitude-based deep learning reconstruction can further significantly reduce MRI scanning time Yang et al. (2024). Therefore, we focus on the task of MRI accelerated reconstruction based on magnitude images, aiming to transform blurry and artifact-ridden MRI images into clear and artifact-free ones. As for accelerated MRI reconstruction based on magnitude images, GAN-based works such as pix2pix Isola et al. (2017), cGAN Zhu et al. (2017) and pGAN Dar et al. (2019) have achieved great progress. Then, diffusion-based methods Song et al. (2020b); Ho et al. (2020) further outperform GANs and improve the reconstruction quality. However, traditional diffusion models (e.g., DDPM Ho et al. (2020) and SDE Song et al. (2020b)) face significant challenges in clinical deployments. Their inference process, which begins with random Gaussian noise, often leads to result instability and requires thousands of sampling steps, resulting in suboptimal reconstruction quality and low efficiency.

To address the above challenge, we first introduce a bridge diffusion model Li et al. (2023); Zhou et al. (2023), where the diffusion process is conducted between two deterministic images and has a clear guarantee to yield the desired conditional distribution without solely relying on a conditional image. To further enhance fine-grained details in reconstructed images and reduce diffusion time steps, we propose a cycle-consistent bridge diffusion method combined with a cycle-consistency loss. This method effectively improves the reconstruction quality of MRI images while significantly reducing the number of diffusion steps. On the other hand, the main difference between under-sampled MR magnitude images and fully-sampled MR magnitude images lies in the structural blurring and artifacts caused by the absence of high-frequency components. Although the iterative sampling process in diffusion models can implicitly capture structural information to a certain extent, it is still insufficient. Therefore, to explicitly account for the structural texture knowledge of MRI images, a Contourlet Decomposition Embedding Module (CDEM) is introduced. By utilizing iterative Laplacian pyramids Burt and Adelson (1987) and directional filter banks Bamberger and Smith (1992);

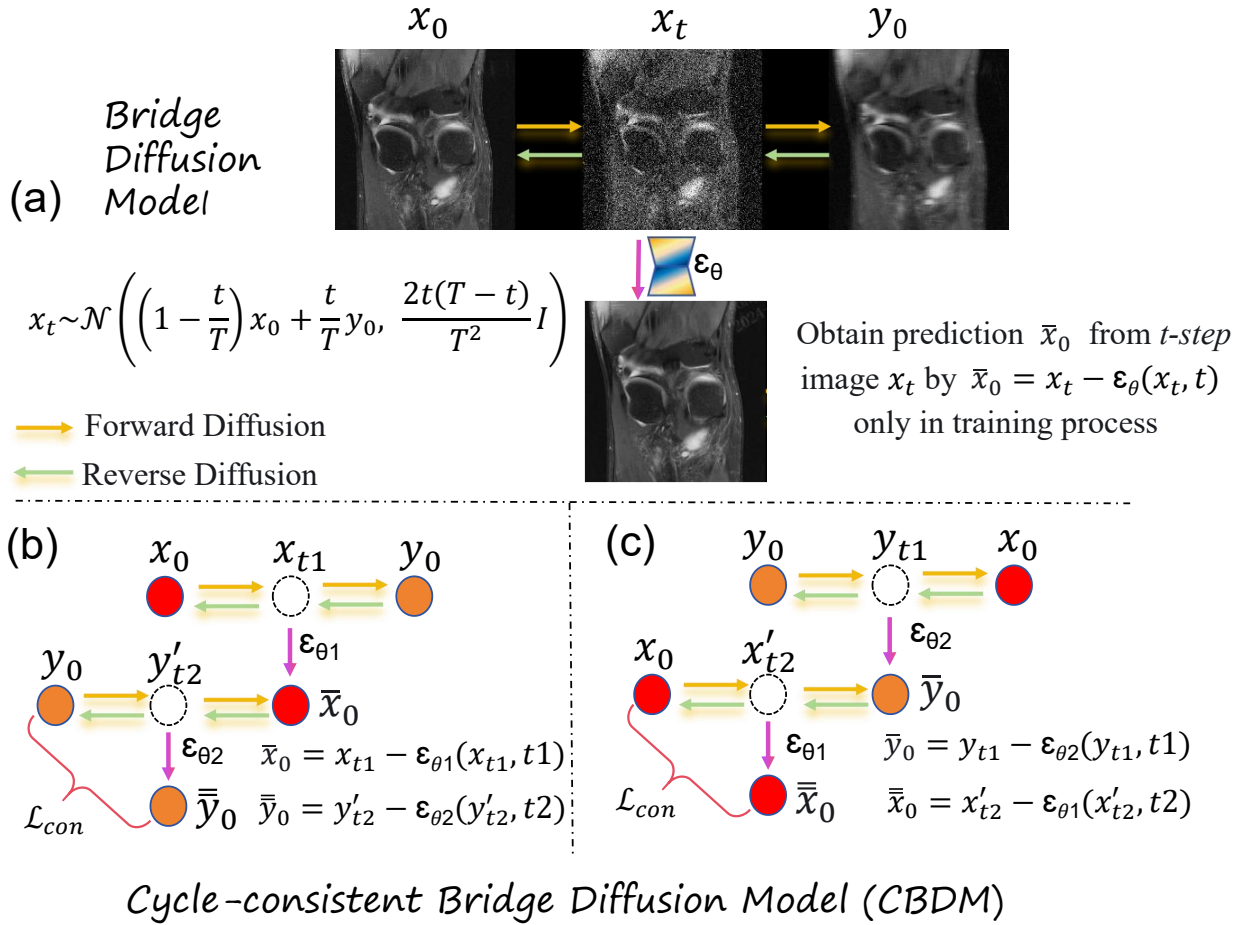


Figure 2: The framework of the CBDM involves cycle-consistent diffusion between deterministically under-sampled and fully-sampled MR magnitude images. (a) A bridge diffusion model. (b) Forward cyclical consistency loss. (c) Backward cyclical consistency loss.

Cimpoi et al. (2015) to decompose the underlying features, this module extracts structural texture knowledge from each time-step image and integrates it into the denoising network, hence enhancing the network’s ability to capture structural textures.

Overall, the contributions of this paper are three-fold:

- 1) We propose a Cycle-Consistent Bridge Diffusion Model (CBDM), which formulates accelerated MRI reconstruction as a cycle-consistent diffusion process between under-sampled and fully-sampled MRI images. This process incorporates a cycle-consistency

loss to preserve fine-grained details and reduce the number of diffusion time steps.

- 2) We propose a contourlet decomposition embedding module that leverages structural texture knowledge extracted from the frequency domain to mitigate the structural discrepancies caused by high-frequency misalignments between under-sampled and fully-sampled MR images.
- 3) Extensive experiments on the public fastMRI and IXI datasets demonstrate the effectiveness of our

proposed Cycle-Consistent Bridge Diffusion-based Model for in-distribution and out-of-distribution accelerated MRI reconstruction.

2. Related works

2.1. Accelerated MRI Reconstruction

For accelerated MRI reconstruction, traditional approaches primarily include Sensitivity Encoding (SENSE) Pruessmann et al. (1999) and GeneRALized Autocalibrating Partially Parallel Acquisitions (GRAPPA) Griswold et al. (2002). SENSE leverages the spatial sensitivity of multiple receiver coils to achieve faster imaging by reducing the acquisition time. On the other hand, GRAPPA reconstructs under-sampled data by estimating missing k-space data using kernel-based interpolation, enhancing the final image quality and reducing artifacts associated with parallel imaging techniques.

With the success of data-driven approaches, deep learning has been widely utilized in accelerated MRI reconstruction. Lv et al. (2021); Sriram et al. (2020) integrate deep learning with parallel imaging algorithms. Sriram et al. (2020) combined deep learning with the GRAPPA reconstruction algorithm. Zhang and Ghanem (2018b) transform the Iterative Shrinkage-Thresholding Algorithm (ISTA) Beck and Teboulle (2009) into a deep neural network to optimize compressive sensing (CS) for accelerated MRI reconstruction. Shitrit and Riklin Raviv (2017) utilized an adversarial neural network to generate the missing k-space data. The generated and missing k-space data are subsequently transformed via Fourier transform and then fed into the discriminator for evaluation. Cole et al. (2020) only requires under-sampled k-space data. The generator produces under-sampled k-space data from the generated image and the discriminator evaluates the k-space measurements instead of the MR image and provides the learned gradients back to the generator. Due to the high-fidelity generation characteristics of diffusion models, they have been widely applied in accelerated MRI reconstruction in recent years. Peng et al. (2022) introduced an unconditional diffusion model, which is trained to generate coil-combined MR image samples derived from fully-sampled data. Gngr et al. (2023) proposed a conditional diffusion model for accelerated MRI reconstruction based on adaptive diffusion priors. To fully utilize the invariant nature of the

low-frequency region in k-space during accelerated sampling, Cao et al. (2024) introduced a conditional diffusion model based on high-frequency diffusion. Similarly, Xie and Li (2022) proposed a measurement-conditioned diffusion model, which avoids diffusion in the undersampled mask region rather than only outside the low-frequency area, thereby preserving more prior information.

Although diffusion models in accelerated MRI reconstruction have evolved from unconditional to conditional and further to prior-based conditional diffusion, they typically set the ending states of the forward diffusion process to pure or partial Gaussian noise instead of a deterministic under-sampled MR image. Differently, our approach leverages the bridge diffusion model to achieve a deterministic image-to-image translation. Then, we propose the cycle-consistent constraint for the model training, further enhancing accelerated MRI reconstruction.

2.2. Diffusion Model

Recent advancements in diffusion models, such as those by Ho et al. (2020); Nichol and Dhariwal (2021); Song et al. (2020b), have significantly enhanced image generation, surpassing the performance of GANs Goodfellow et al. (2014). These successes are attributed to key design choices, including network architecture Song et al. (2020b); Karras et al. (2022), optimized noise schedules Nichol and Dhariwal (2021); Karras et al. (2022), improved sampling techniques Song et al. (2020a); Lu et al. (2022); Zhang and Chen (2022), and advanced guidance methods Nichol and Dhariwal (2021); Ho and Salimans (2022).

Bridge diffusion models Li et al. (2023); Zhou et al. (2023) have been proposed for image translation tasks, where the diffusion process is constructed between paired images. This approach starts reverse diffusion from a deterministic image (without noise), making the sampling process more stable. Inspired by the bridge diffusion model, we construct a cycle-consistent bridge diffusion model between under-sampled and fully-sampled MR magnitude images.

3. Method

Fig. 2 shows an overview of our Cycle-Consistent Bridge Diffusion Model, including two bridge diffusion

models for transformations $\mathbf{x} \leftarrow \mathbf{y}$ and $\mathbf{y} \leftarrow \mathbf{x}$, respectively. Here, \mathbf{x}_0 and \mathbf{y}_0 denote the fully-sampled and under-sampled magnitude images. \rightarrow and \leftarrow denote the forward and reverse processes in each diffusion model, respectively.

3.1. Bridge Diffusion Model

Given the inconsistent predictions of typical diffusion models, we exploit the Brownian bridge diffusion model Li et al. (2023) for the deterministic image-to-image transformation. The state distribution at each time step t of a forward process ((e.g.,) $\mathbf{x} \rightarrow \mathbf{y}$) can be expressed as:

$$q(\mathbf{x}_t|\mathbf{x}_0, \mathbf{y}_0) = N(\mathbf{x}_t; (1 - m_t)\mathbf{x}_0 + m_t\mathbf{y}_0, \sigma_t \mathbf{I}) \quad (1)$$

$$m_t = \frac{t}{T}, \sigma_t = 2(m_t - (m_t)^2)$$

where $\mathbf{x}_0 \sim \mathbf{q}_{data}(\mathbf{x}_0)$, and $\mathbf{y}_0 \sim \mathbf{q}_{data}(\mathbf{y}_0)$. T is the total number of iteration steps and σ_t denotes the variance. Here, the variances at the starting and ending states, (i.e.,) σ_0 and σ_T are 0, avoiding the random predictions. Meanwhile, $\sigma_{T/2} = 0.5$ is bounded, which could smooth the model training Li et al. (2023).

The intermediate state \mathbf{x}_t in the forward process, transitioning from the starting state \mathbf{x}_0 to the ending state \mathbf{y}_0 , can be represented as

$$\mathbf{x}_t = (1 - m_t)\mathbf{x}_0 + m_t\mathbf{y}_0 + \sqrt{\sigma_t}\boldsymbol{\epsilon} \quad (2)$$

where $\boldsymbol{\epsilon} \sim \mathcal{N}(\mathbf{0}, \mathbf{I})$.

Then, for the reverse process, the Brownian Bridge model initiates directly from image \mathbf{y}_0 . Following the principle of denoising diffusion methods, the reverse process ($\mathbf{x} \leftarrow \mathbf{y}$) aims to predict \mathbf{x}_{t-1} based on \mathbf{x}_t :

$$\begin{aligned} p_\theta(\mathbf{x}_{t-1}|\mathbf{x}_t, \mathbf{y}_0) &= \mathcal{N}(\mathbf{x}_{t-1}; \boldsymbol{\mu}_\theta(\mathbf{x}_t, t), \tilde{\sigma}_t \mathbf{I}) \\ \text{s.t., } \tilde{\sigma}_t &= \sigma_{t|t-1} \frac{\sigma_{t-1}}{\sigma_t} \\ \sigma_{t|t-1} &= \sigma_t - \sigma_{t-1} \frac{(1 - m_t)^2}{(1 - m_{t-1})^2} \end{aligned} \quad (3)$$

where $\boldsymbol{\mu}_\theta(\mathbf{x}_t, t)$ represents the predicted mean value of noise at the t -th steps, and $\tilde{\sigma}_t$ denotes noise variances in the reverse process.

Finally, the loss function is formulated by optimizing the Evidence Lower Bound (ELBO) for the Brownian

Bridge diffusion process:

$$\mathbb{E}_{\mathbf{x}_0, \mathbf{y}_0, \boldsymbol{\epsilon}}[\underbrace{\|(m_t(\mathbf{y}_0 - \mathbf{x}_0) + \sqrt{\sigma_t}\boldsymbol{\epsilon}) - \boldsymbol{\epsilon}_\theta(\mathbf{x}_t, t)\|}_{\text{objective}}] \quad (4)$$

Therefore, let $\boldsymbol{\theta}_1$ and $\boldsymbol{\theta}_2$ represent the denoising networks for $\mathbf{x} \leftarrow \mathbf{y}$ and $\mathbf{y} \leftarrow \mathbf{x}$ processes, respectively. The diffusion losses $\mathcal{L}_{\mathbf{x} \leftarrow \mathbf{y}}^{rec}$ and $\mathcal{L}_{\mathbf{y} \leftarrow \mathbf{x}}^{rec}$ at step t are:

$$\begin{aligned} \mathcal{L}_{\mathbf{x} \leftarrow \mathbf{y}}^{rec} &= \mathbb{E}_{\mathbf{x}_0, \mathbf{y}_0, \boldsymbol{\epsilon}}[\|(m_t(\mathbf{y}_0 - \mathbf{x}_0) + \sqrt{\sigma_t}\boldsymbol{\epsilon}) - \boldsymbol{\epsilon}_{\theta_1}(\mathbf{x}_t, t)\|] \\ \mathcal{L}_{\mathbf{y} \leftarrow \mathbf{x}}^{rec} &= \mathbb{E}_{\mathbf{y}_0, \mathbf{x}_0, \boldsymbol{\epsilon}}[\|(m_t(\mathbf{x}_0 - \mathbf{y}_0) + \sqrt{\sigma_t}\boldsymbol{\epsilon}) - \boldsymbol{\epsilon}_{\theta_2}(\mathbf{y}_t, t)\|]. \end{aligned} \quad (5)$$

Note that, Equation (4) theoretically indicates that with sufficiently low loss, the original target image \mathbf{x}_0 can be estimated at any time t given a noisy image \mathbf{x}_t . Therefore, the reconstructed $\bar{\mathbf{x}}_0$ based on \mathbf{y}_0 at t step can be calculated using the generation function only in training process:

$$\bar{\mathbf{x}}_0 = \mathbf{x}_t - \boldsymbol{\epsilon}_\theta(\mathbf{x}_t, t) \quad (6)$$

Note, the $\bar{\mathbf{x}}_0$ obtained during inference is generated through inverse diffusion sampling, following the same sampling procedure as described in Li et al. (2023).

3.2. Cycle-Consistent Bridge Diffusion Model

To enhance the diffusion model training, we further adopt a cyclical design. Specifically, Equation (6) indicates that, during training, the target image \mathbf{x}_0 or \mathbf{y}_0 can be estimated by a noisy state \mathbf{x}_{t1} and \mathbf{y}_{t1} , respectively. Therefore, the reconstructed fully-sampled and under-sampled MR magnitude images $\bar{\mathbf{x}}_0$ and $\bar{\mathbf{y}}_0$ become:

$$\begin{aligned} \bar{\mathbf{x}}_0 &= \mathbf{x}_{t1} - \boldsymbol{\epsilon}_{\theta_1}(\mathbf{x}_{t1}, t1) \\ \bar{\mathbf{y}}_0 &= \mathbf{x}_{t1} - \boldsymbol{\epsilon}_{\theta_2}(\mathbf{y}_{t1}, t1). \end{aligned} \quad (7)$$

We then set the reconstructed ones as new end states. Hence, the intermediate states \mathbf{x}'_{t2} and \mathbf{y}'_{t2} become:

$$\begin{aligned} \mathbf{y}'_{t2} &= (1 - m_{t2})\mathbf{y}_0 + m_{t2}\bar{\mathbf{x}}_0 + \sqrt{\sigma_{t2}}\boldsymbol{\epsilon} \\ \mathbf{x}'_{t2} &= (1 - m_{t2})\mathbf{x}_0 + m_{t2}\bar{\mathbf{y}}_0 + \sqrt{\sigma_{t2}}\boldsymbol{\epsilon}. \end{aligned} \quad (8)$$

Similarly, the reverse processes $\mathbf{y} \leftarrow \bar{\mathbf{x}}_0$ and $\mathbf{x} \leftarrow \bar{\mathbf{y}}_0$ can obtain the new reconstructed images $\bar{\bar{\mathbf{y}}}_0$ and $\bar{\bar{\mathbf{x}}}_0$, respectively as:

$$\begin{aligned} \bar{\bar{\mathbf{y}}}_0 &= \mathbf{y}'_{t2} - \boldsymbol{\epsilon}_{\theta_2}(\mathbf{y}'_{t2}, t2) \\ \bar{\bar{\mathbf{x}}}_0 &= \mathbf{x}'_{t2} - \boldsymbol{\epsilon}_{\theta_1}(\mathbf{x}'_{t2}, t2). \end{aligned} \quad (9)$$

Therefore, a cycle-consistency loss can be used to reduce the distance between \mathbf{x}_0 and $\bar{\mathbf{x}}_0$, and between \mathbf{y}_0 and $\bar{\mathbf{y}}_0$, respectively as:

$$\begin{aligned}\mathcal{L}_x^{con}(\theta_1, \theta_2) &= \mathbb{E}_{\mathbf{x}_0, \mathbf{y}_0} [\|\mathbf{x}_0 - \bar{\mathbf{x}}_0\|] \\ \mathcal{L}_y^{con}(\theta_1, \theta_2) &= \mathbb{E}_{\mathbf{x}_0, \mathbf{y}_0} [\|\mathbf{y}_0 - \bar{\mathbf{y}}_0\|].\end{aligned}\quad (10)$$

Overall, the total loss is a weighted sum of construction loss and consistency losses as

$$\mathcal{L}_{total} = \lambda(\mathcal{L}_x^{con} + \mathcal{L}_y^{con}) + (\mathcal{L}_{x \leftarrow y}^{rec} + \mathcal{L}_{y \leftarrow x}^{rec}) \quad (11)$$

where λ is a constant to balance losses for the model training. Algorithm 1 shows pseudo codes of our algorithm. Note that, only a denoising network θ_1 is used for the model inference. Here, the model does not introduce additional inference time.

Algorithm 1 Pseudo training codes of our cycle-consistent bridge diffusion model for accelerated MRI reconstruction

- 1: **repeat**
 - 2: Paired data $\mathbf{x}_0 \sim q(\mathbf{x}_0)$, $\mathbf{y}_0 \sim q(\mathbf{y}_0)$
 - 3: Timestep $t_1 \sim Uniform(1, \dots, T)$
 - 4: Timestep $t_2 \sim Uniform(1, \dots, T)$
 - 5: Gaussian noise $\epsilon \sim \mathcal{N}(\mathbf{0}, \mathbf{I})$
 - 6: Forward diffusion $\mathbf{x}_0 \rightarrow \mathbf{y}_0$
 $\quad \mathbf{x}_{t_1} = (1 - m_{t_1})\mathbf{x}_0 + m_{t_1}\mathbf{y}_0 + \sqrt{\sigma_{t_1}}\epsilon$
 - 7: Computing $\bar{\mathbf{x}}_0 = \mathbf{x}_{t_1} - \epsilon_{\theta_1}(\mathbf{x}_{t_1}, t_1)$
 - 8: Forward diffusion $\mathbf{y}_0 \rightarrow \mathbf{x}_0$
 $\quad \mathbf{y}_{t_1} = (1 - m_{t_1})\mathbf{y}_0 + m_{t_1}\mathbf{x}_0 + \sqrt{\sigma_{t_1}}\epsilon$
 - 9: Computing $\bar{\mathbf{y}}_0 = \mathbf{y}_{t_1} - \epsilon_{\theta_2}(\mathbf{y}_{t_1}, t_1)$
 - 10: Forward diffusion $\mathbf{y}_0 \rightarrow \bar{\mathbf{x}}_0$
 $\quad \mathbf{y}'_{t_2} = (1 - m_{t_2})\mathbf{y}_0 + m_{t_2}\bar{\mathbf{x}}_0 + \sqrt{\sigma_{t_2}}\epsilon$
 - 11: Computing $\bar{\bar{\mathbf{y}}}_0 = \mathbf{y}'_{t_2} - \epsilon_{\theta_2}(\mathbf{y}'_{t_2}, t_2)$
 - 12: Forward diffusion $\mathbf{x}_0 \rightarrow \bar{\mathbf{y}}_0$
 $\quad \mathbf{x}'_{t_2} = (1 - m_{t_2})\mathbf{x}_0 + m_{t_2}\bar{\mathbf{y}}_0 + \sqrt{\sigma_{t_2}}\epsilon$
 - 13: Computing $\bar{\bar{\mathbf{x}}}_0 = \mathbf{x}'_{t_2} - \epsilon_{\theta_1}(\mathbf{x}'_{t_2}, t_2)$
 Take gradient descent step on
 - 14: $\nabla_{\theta_1} \|(m_{t_1}(\mathbf{y}_0 - \mathbf{x}_0) + \sqrt{\sigma_{t_1}}\epsilon) - \epsilon_{\theta_1}(\mathbf{x}_{t_1}, t_1)\|$
 $\quad \nabla_{\theta_2} \|(m_{t_1}(\mathbf{x}_0 - \mathbf{y}_0) + \sqrt{\sigma_{t_1}}\epsilon) - \epsilon_{\theta_2}(\mathbf{y}_{t_1}, t_1)\|$
 $\quad \nabla_{\theta_1, \theta_2} \|\mathbf{y}_0 - \bar{\mathbf{y}}_0\|$
 $\quad \nabla_{\theta_1, \theta_2} \|\mathbf{x}_0 - \bar{\bar{\mathbf{x}}}_0\|$
 - 15: **until**
-

3.3. Contourlet Decomposition Embedding Module

The denoising networks of our CBDM model adopt a U-Net Ronneberger et al. (2015) with a time embedding. As illustrated in Fig. 3, we further propose a contourlet decomposition embedding module to enhance the backbone. Generally, the blurring and artifacts in under-sampled MR magnitude images are caused by the missing high-frequency information in the frequency space. Contourlet decomposition employs the Laplacian Pyramid (LP) Burt and Adelson (1987) and Directional Filter Banks (DFB) Bamberger and Smith (1992); Cimpoi et al. (2015) to process the low-pass images iteratively. LP aims to achieve low- and high-frequency decomposition in a multi-scale fashion. DFB is used to reconstruct the original signal with minimal samples, producing minimal sample representations in the 2D frequency domain through j -level binary tree decomposition, resulting in 2^j directional sub-bands.

For example, the frequency domain is divided into 2^3 directional sub-bands when $j = 3$, and sub-bands 0 – 3 and 4 – 7 correspond to the vertical and horizontal details, respectively. Fig 4 illustrates the visualization of sub-band features at different levels obtained from the contourlet decomposition of x_t . It can be observed that contourlet decomposition effectively extracts high-frequency features of image edges. Then, the Contourlet Decomposition Embedding Module further resizes the features of multiple sub-bands at each level to match the feature size at the corresponding level, stacks them along the channel dimension, and then uses three convolution layers to align the channel number as corresponding level features.

4. Experiments

4.1. Data and Implementation Details

The experiments were conducted on the public benchmark fastMRI¹ and IXI datasets². From the fastMRI dataset, we selected 360 individuals from the multi-coil knee dataset for training, 8 for validation, and 20 for testing. Following Cao et al. (2024), the first six slices of each individual were excluded due to poor image quality.

¹<http://fastmri.med.nyu.edu>

²<https://brain-development.org/ixi-dataset/>

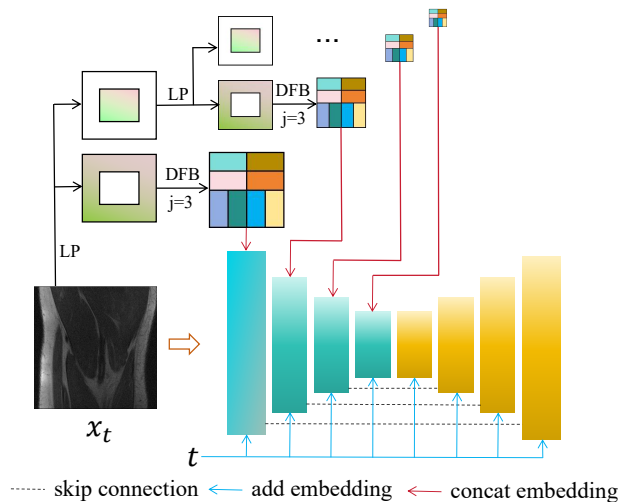


Figure 3: Denosing network with time and contourlet decomposition embedding.

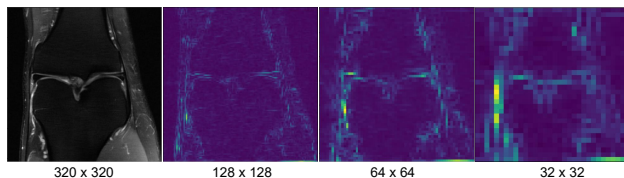


Figure 4: Contourlet decomposition features visualization with different level.

Consequently, the training, validation, and test sets contained 10,737, 244, and 576 2D images, respectively. Additionally, 218 images from 20 individuals in the fastMRI brain dataset were selected as an out-of-distribution set of images. All images were cropped to 320×320 and normalized to the range $[0, 1]$. From the IXI dataset, we selected 577 patients with T1 images, randomly split into training (500 patients, 44,935 2D images), validation (37 patients, 3,330 images), and test (40 patients, 3,600 images) sets. All images were cropped to 256×256 and normalized to the range $[0, 1]$. To simulate k-space undersampling, equally spaced Cartesian undersampling in the phase encoding direction was applied, with acceleration factors set to 4 and 8. The final MR magnitude images, both under-sampled and fully sampled, were gener-

Sampling	Type	Method	PSNR(dB) \uparrow	SSIM(%) \uparrow	NMSE(%) \downarrow
Equi 4	GAN	pGAN(2019)	29.72 \pm 1.79	79.63 \pm 7.09	4.78 \pm 4.15
		cGAN(2017)	30.14 \pm 2.17	81.83 \pm 5.91	4.71 \pm 4.73
		pix2pix(2017)	32.64 \pm 2.26	86.76 \pm 6.20	3.01 \pm 3.46
	Diffusion	DDPM(2020)	32.78 \pm 2.87	86.84 \pm 8.06	3.36 \pm 4.54
		IDDPM(2021)	32.78 \pm 2.82	86.90 \pm 8.11	3.29 \pm 4.47
		AdaDiff(2023)	28.16 \pm 1.94	78.77 \pm 5.03	6.60 \pm 3.56
		MC-DDPM(2022)	33.84 \pm 3.38	88.24\pm3.57	3.02 \pm 3.05
		HFS-SDE(2024)	30.70 \pm 2.10	82.19 \pm 5.36	3.79 \pm 3.24
BBDM(2023)	33.79 \pm 2.48	87.85 \pm 7.19	<u>2.47\pm3.04</u>		
CBDM(Ours)	34.84\pm2.48	89.73\pm6.20	1.96\pm2.40		
Equi 8	GAN	pGAN(2019)	27.23 \pm 1.82	71.34 \pm 8.47	7.55 \pm 5.28
		cGAN(2017)	27.96 \pm 2.07	75.16 \pm 7.23	7.43 \pm 7.09
		pix2pix(2017)	30.80 \pm 2.00	82.44 \pm 6.95	4.29 \pm 4.50
	Diffusion	DDPM(2020)	30.36 \pm 2.79	81.45 \pm 9.06	5.44 \pm 8.59
		IDDPM(2021)	30.84 \pm 2.44	81.87 \pm 8.92	4.60 \pm 5.40
		AdaDiff(2023)	28.85 \pm 2.15	77.53 \pm 6.15	6.04 \pm 4.58
		MC-DDPM(2022)	31.30 \pm 2.45	84.58\pm5.84	3.30 \pm 2.79
		HFS-SDE(2024)	28.14 \pm 2.03	75.52 \pm 5.20	5.86 \pm 3.84
BBDM(2023)	<u>31.68\pm2.14</u>	83.39 \pm 8.02	<u>3.63\pm4.00</u>		
CBDM(Ours)	32.80\pm2.20	85.83\pm6.97	2.96\pm3.37		

Table 1: Comparison of methods in in-distribution fastMRI knee experiments. *Equi 4* and *Equi 8* represent equally-spaced Cartesian undersampling with acceleration factors of 4 and 8, respectively. **Bold** and **underline** indicate the best and second-best results, respectively.

ated from the corresponding k-space data through inverse Fourier transform and root sum of squares operations.

For training, the total number of iterations is 200k, using the AdamW optimizer with a learning rate of $1e-4$ and a batch size of 28. For other diffusion methods (excluding AdaDiff), the training and sampling steps are set to 1000 and 200, respectively. In AdaDiff, the first stage employs an unconditional pretraining diffusion model with 1000 time steps, while the second stage uses 200 steps for iterative solving based on data consistency Zheng et al. (2019). For our CBDM, both the training and sampling steps are set to 20, with the loss weight λ set to 1. To ensure fairness, all diffusion models use the same network architecture. All experiments were conducted in the same environment using 4 NVIDIA Tesla V100 GPUs.

The comparison was conducted by the proposed CBDM model and pGAN Dar et al. (2019), cGAN Zhu et al. (2017), pix2pix Isola et al. (2017), DDPM Ho et al. (2020), IDDPM Nichol and Dhariwal (2021), AdaDiff GÜngör et al. (2023), MC-DDPM Xie and Li (2022), HFS-SDE Cao et al. (2024) and BBDM Li et al. (2023). We further use the widely used Peak Signal-to-Noise Ratio (PSNR), Structural Similarity Index (SSIM) and Normalized Mean Square Error (NMSE) for the measurement of reconstruction quality.

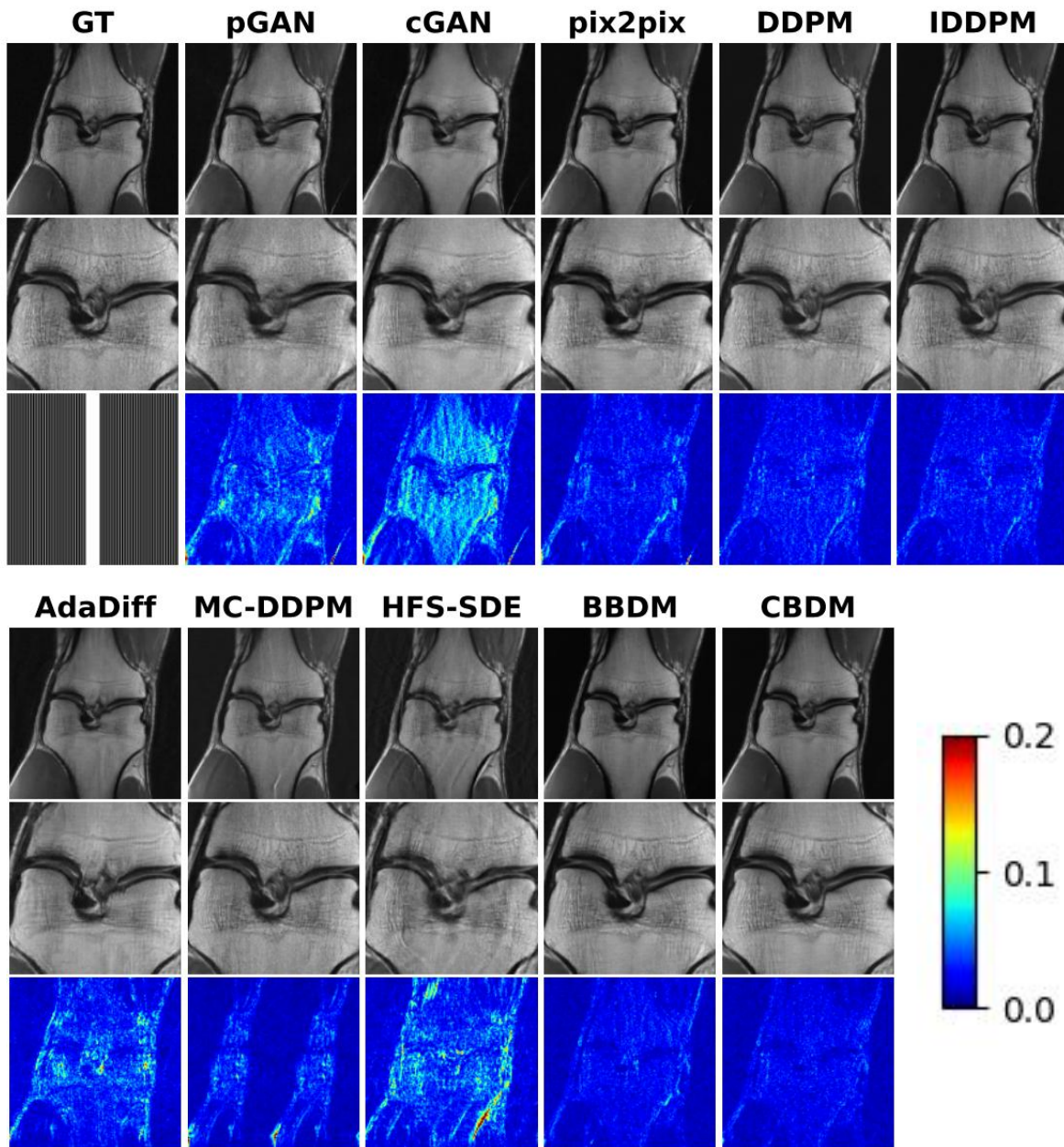


Figure 5: The reconstruction results (in-distribution) of fastMRI multi-coil knee data at equally-spaced Cartesian undersampling with an acceleration factor of 4 are shown. The first row displays the ground truth and the reconstructions from pGAN, cGAN, pix2pix, DDPM, IDDPM, AdaDiff, MC-DDPM, HFS-SDE and CBDM (Ours). The second row presents the enlarged view of the ROI, and the third row shows the error map of the reconstruction. The lower left corner contains the undersampling mask.

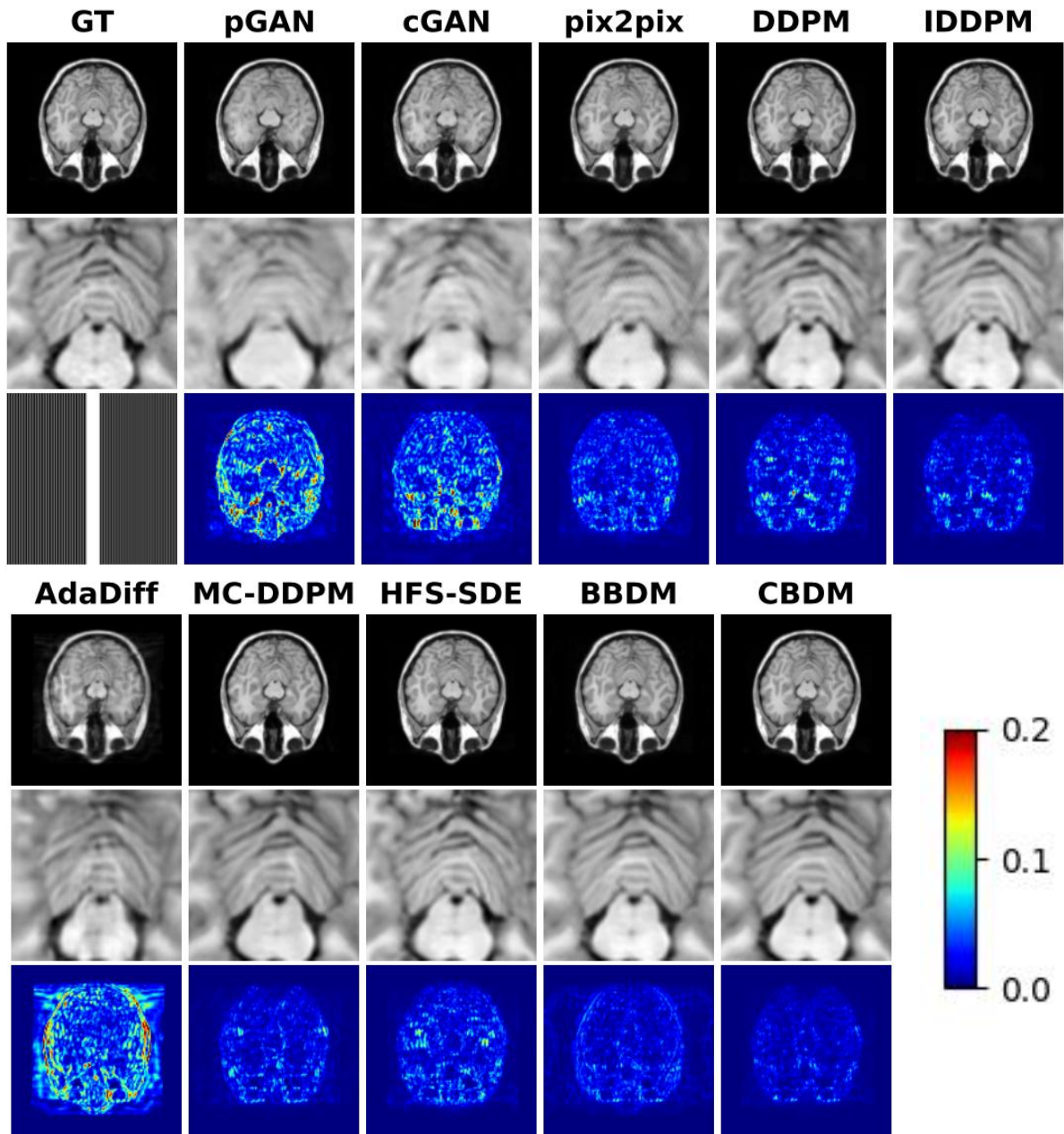


Figure 6: The reconstruction results of in-distribution IXI brain data at equally-spaced Cartesian undersampling with an acceleration factor of 4 are shown. The first row displays the ground truth and the reconstructions from pGAN, cGAN, pix2pix, DDPM, IDDPM, AdaDiff, MC-DDPM, HFS-SDE and CBDM (Ours). The second row presents the enlarged view of the ROI, and the third row shows the error map of the reconstruction. The lower left corner contains the undersampling mask.

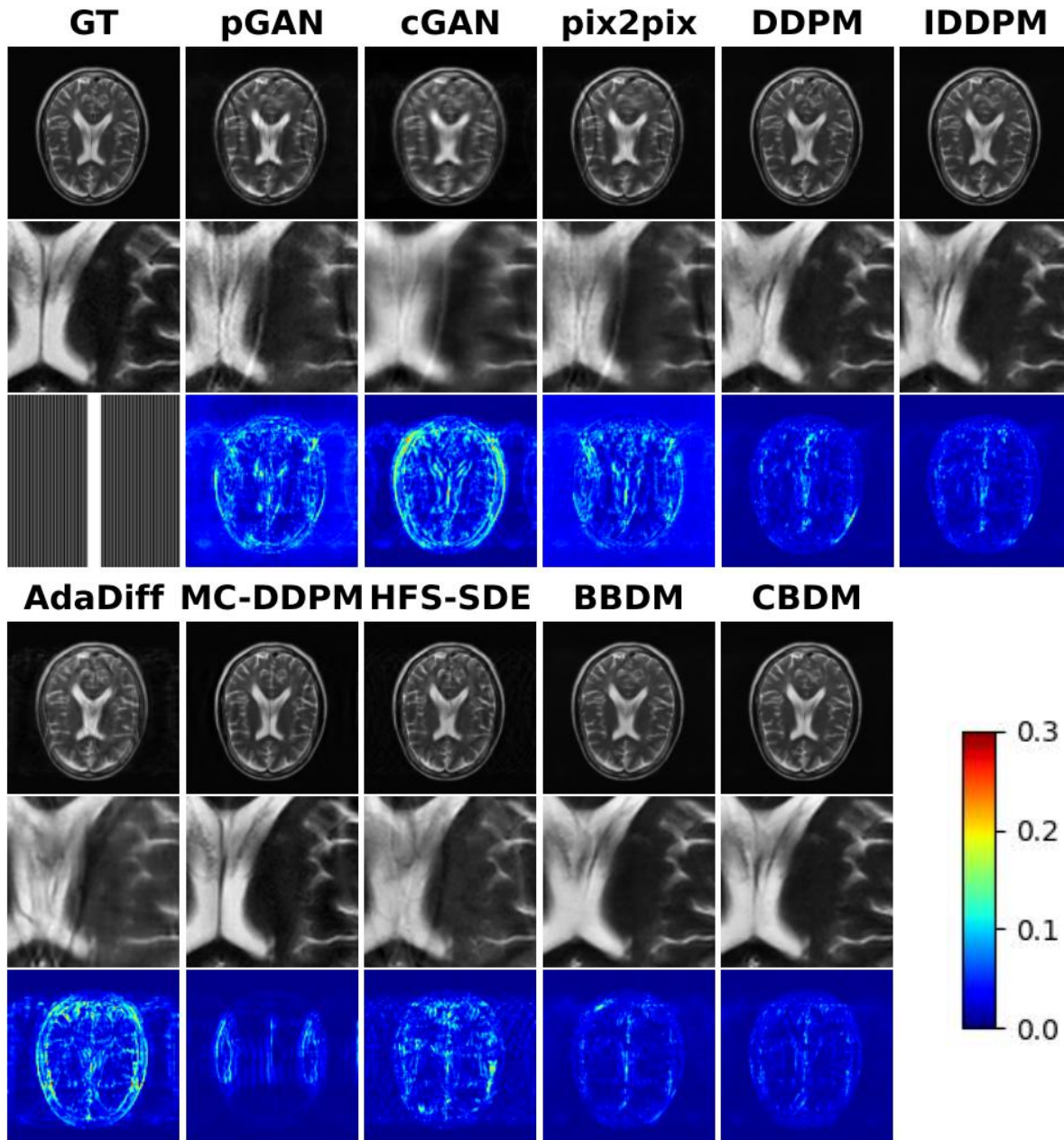


Figure 7: The reconstruction results (out-of-distribution) of fastMRI multi-coil brain data at equally-spaced Cartesian undersampling with an acceleration factor of 4 are shown. The first row displays the ground truth and the reconstructions from pGAN, cGAN, pix2pix, DDPM, IDDPM, AdaDiff, MC-DDPM, HFS-SDE and CBDM (Ours). The second row presents the enlarged view of the ROI, and the third row shows the error map of the reconstruction. The lower left corner contains the undersampling mask.

4.2. In-Distribution Results

Regarding the fastMRI Knee dataset and the IXI dataset, as shown in Table 1 and 2, under equally-spaced Cartesian sampling with $4\times$ and $8\times$ acceleration, our CBDM consistently outperforms all other methods across all metrics on both in-distribution datasets. Compared to state-of-the-art diffusion models, MC-DDPM Xie and Li (2022) and BBDM Li et al. (2023), our method achieves a $\sim 1\text{dB}$ improvement in PSNR and a $\sim 1\%-2\%$ increase in SSIM. The reconstruction results of the fastMRI knee dataset under $4\times$ equally-spaced Cartesian sampling are shown in Fig. 5. The first row includes results from pGAN, cGAN, pix2pix, DDPM, IDDPM, AdaDiff, MC-DDPM, HFS-SDE, BBDM, and CBDM. The second row displays the enlarged views of regions of interest (ROI), while the third row shows the error heatmaps. HFS-SDE exhibits noise and aliasing artifacts in the reconstructions due to the small center size of the low-frequency region. Similarly, the reconstructed images from pGAN, cGAN, AdaDiff, pix2pix, and MC-DDPM exhibit significant artifacts and noise, resulting in the loss of certain structures. In contrast, DDPM, IDDPM, BBDM, and our CBDM preserve more details. Among these, CBDM excels in reconstruction by preserving the most realistic high-frequency details and effectively suppressing artifacts. Fig. 6 presents the reconstruction results of the IXI dataset under a $4\times$ equally-spaced Cartesian sampling mask. CBDM similarly achieves the best performance, retaining the most realistic details to deliver the best visual quality.

4.3. Out-of-Distribution Results

We further conducted out-of-distribution experiments to verify the generalization of our model. All models were trained on fastMRI knee data and tested by fastMRI brain MRI scans. The reconstruction results for equally-spaced Cartesian sampling with $4\times$ acceleration are shown in Fig. 7. The reconstruction quality of pGAN, cGAN, and pix2pix methods significantly decreased, whereas diffusion-based methods maintained good reconstruction quality. Among them, our CBDM achieved the optimal reconstruction results with fewer noise and artifacts. Table 3 gives quantitative performance for the out-of-distribution experiments and our proposed CBDM model achieves the best performance for the brain data reconstruction.

Sampling	Type	Method	PSNR(dB) \uparrow	SSIM(%) \uparrow	NMSE(%) \downarrow
Equi 4	GAN	pGAN(2019)	28.46 \pm 1.43	87.01 \pm 1.92	1.93 \pm 0.77
		cGAN(2017)	27.68 \pm 1.64	86.49 \pm 1.95	2.38 \pm 0.98
		pix2pix(2017)	30.56 \pm 1.60	87.66 \pm 1.41	1.24 \pm 0.53
	Diffusion	DDPM(2020)	32.70 \pm 2.77	95.32 \pm 2.10	0.85 \pm 0.59
		IDDPM(2021)	35.11 \pm 3.09	96.89 \pm 1.60	0.51 \pm 0.40
		AdaDiff(2023)	25.84 \pm 1.28	80.09 \pm 3.71	3.92 \pm 1.41
		MC-DDPM(2022)	36.20 \pm 3.11	97.49 \pm 1.31	0.37 \pm 0.30
		HFS-SDE(2024)	30.76 \pm 2.80	89.22 \pm 2.15	1.16 \pm 0.60
		BBDM(2023)	36.57 \pm 3.10	97.70 \pm 1.25	0.36 \pm 0.29
		CBDM(Ours)	37.56\pm3.07	98.10\pm1.02	0.29\pm0.22
Equi 8	GAN	pGAN(2019)	24.15 \pm 5.28	89.75 \pm 1.84	5.01 \pm 1.33
		cGAN(2017)	25.84 \pm 1.47	82.90 \pm 3.98	3.70 \pm 1.38
		pix2pix(2017)	31.12 \pm 1.96	93.94 \pm 2.01	1.12 \pm 0.55
	Diffusion	DDPM(2020)	32.56 \pm 2.72	95.02 \pm 2.21	0.87 \pm 0.60
		IDDPM(2021)	34.89 \pm 3.02	96.53 \pm 1.73	0.53 \pm 0.40
		AdaDiff(2023)	23.74 \pm 1.05	75.45 \pm 3.87	6.45 \pm 1.86
		MC-DDPM(2022)	35.53 \pm 2.96	97.04 \pm 1.53	0.45 \pm 0.34
		HFS-SDE(2024)	30.47 \pm 2.46	92.96 \pm 2.27	1.08 \pm 0.45
		BBDM(2023)	35.75 \pm 2.97	97.10 \pm 1.46	0.43 \pm 0.33
		CBDM(Ours)	37.09\pm2.96	97.70\pm1.15	0.32\pm0.23

Table 2: Comparison of methods in in-distribution IXI experiments. *Equi 4* and *Equi 8* represent equally-spaced Cartesian undersampling with acceleration factors of 4 and 8, respectively. **Bold** and **underline** indicate the best and second-best results, respectively.

Sampling	Type	Method	PSNR(dB) \uparrow	SSIM(%) \uparrow	NMSE(%) \downarrow
Equi 4	GAN	pGAN(2019)	26.14 \pm 1.22	76.34 \pm 4.71	8.35 \pm 2.84
		cGAN(2017)	26.48 \pm 1.80	84.04 \pm 3.87	7.65 \pm 3.45
		pix2pix(2017)	27.09 \pm 1.36	81.89 \pm 4.62	6.84 \pm 2.53
	Diffusion	DDPM(2020)	29.71 \pm 1.85	90.38 \pm 2.11	3.76 \pm 1.43
		IDDPM(2021)	29.68 \pm 1.80	90.31 \pm 2.12	3.68 \pm 1.27
		AdaDiff(2023)	24.93 \pm 1.30	81.21 \pm 3.07	13.2 \pm 4.37
		MC-DDPM(2022)	29.93 \pm 1.76	90.47 \pm 2.14	3.11 \pm 0.85
		HFS-SDE(2024)	26.03 \pm 1.35	79.69 \pm 3.58	7.40 \pm 1.34
		BBDM(2023)	29.41 \pm 1.64	91.01 \pm 1.78	3.16 \pm 1.12
		CBDM(Ours)	30.67\pm1.71	91.97\pm1.42	2.98\pm0.94
Equi 8	GAN	pGAN(2019)	24.15 \pm 1.06	71.10 \pm 5.19	12.5 \pm 3.27
		cGAN(2017)	25.42 \pm 1.01	82.08 \pm 3.32	9.00 \pm 2.34
		pix2pix(2017)	25.72 \pm 1.13	79.32 \pm 4.71	9.41 \pm 2.69
	Diffusion	DDPM(2020)	27.47 \pm 1.30	86.93 \pm 2.23	6.15 \pm 1.56
		IDDPM(2021)	27.36 \pm 1.30	86.95 \pm 2.19	6.35 \pm 1.64
		AdaDiff(2023)	25.67 \pm 1.37	80.08 \pm 3.13	10.0 \pm 2.72
		MC-DDPM(2022)	26.10 \pm 2.21	82.52 \pm 3.56	7.91 \pm 2.89
		HFS-SDE(2024)	24.81 \pm 1.39	73.87 \pm 4.14	9.55 \pm 2.03
		BBDM(2023)	27.56 \pm 1.30	86.95 \pm 2.19	6.35 \pm 1.64
		CBDM(Ours)	28.65\pm1.24	89.02\pm1.94	4.62\pm1.20

Table 3: Comparison of methods in out-of-distribution fastMRI brain experiments, using models trained on the in-distribution fastMRI knee dataset. *Equi 4* and *Equi 8* represent equally-spaced Cartesian undersampling with acceleration factors of 4 and 8, respectively. **Bold** and **underline** indicate the best and second-best results, respectively.

Cycle-Consistent	CDEM	PSNR(dB) \uparrow	SSIM(%) \uparrow	NMSE(%) \downarrow
		33.79 \pm 2.48	87.85 \pm 7.19	2.47 \pm 3.04
	✓	34.15 \pm 2.53	88.25 \pm 7.19	2.32 \pm 2.86
✓		34.62 \pm 2.49	89.56 \pm 6.19	2.04 \pm 2.47
✓	✓	34.84\pm2.54	89.73\pm6.20	1.96\pm2.40

Table 4: Ablation studies of different components. We report the metrics on fastMRI knee dataset under the *Equi 4*.

$t1 = t2 \sim U$	$t1 \sim U, t2 \sim U$	PSNR(dB) \uparrow	SSIM(%) \uparrow	NMSE(%) \downarrow
✓		34.84 \pm 2.54	89.73 \pm 6.20	1.96 \pm 2.40
	✓	34.85 \pm 2.55	89.75 \pm 6.16	1.96 \pm 2.39

Table 5: Ablation studies of different time steps in $x_0/y_0 \rightarrow y_0/x_0$ and $y_0/x_0 \rightarrow \bar{x}_0/\bar{y}_0$. U denotes a uniform distribution $Uniform(1, \dots, T)$.

$\sqrt{\sigma_{t1}}$	$\sqrt{\sigma_{t2}}$	PSNR(dB) \uparrow	SSIM(%) \uparrow	NMSE(%) \downarrow
1.0	1.0	34.67 \pm 2.50	89.54 \pm 6.20	2.03 \pm 2.49
1.0	1.1	34.79 \pm 2.54	89.73 \pm 6.19	1.97 \pm 2.41
1.0	1.2	34.84\pm2.54	89.73\pm6.20	1.96\pm2.40
1.0	1.3	34.76 \pm 2.56	89.70 \pm 6.19	2.00 \pm 2.47

Table 6: Ablation studies of different noise variances.

4.4. Inference Efficiency

In the above experiments, the training and sampling steps for CBDM were set to 20 each, while other diffusion methods (except AdaDiff) used 1000 training steps and 200 sampling steps. The 200 sampling steps were accelerated using DDIM Song et al. (2020a) sampling. For AdaDiff, the first stage involved pretraining with 1000 steps, and the second stage did not use 200 sampling steps but instead performed 200 online iterations based on the data consistency loss. As shown in Fig. 8 (a), CBDM’s significantly reduced sampling steps result in much higher inference efficiency compared to other diffusion methods.

To further compare inference efficiency fairly, we also set the sampling steps or the second-stage iteration steps of other methods to 20, as shown in Fig. 8 (b). This adjustment led to a substantial drop in reconstruction performance for these methods. Although using DDIM Song et al. (2020a) with very few sampling steps can improve sampling speed, it comes with significant performance degradation, making it impractical for real-world applications. In contrast, CBDM achieves both training and sampling with only 20 steps, maintaining high efficiency without compromising reconstruction performance.

4.5. Ablation Study

Table 4 shows an ablation study to verify the effectiveness of our designs. The traditional BBDM Li et al. (2023) model is set as the baseline. Results indicate that BBDM achieves better results than other diffusion models. Then, both the cycle-consistency and CDEM designs improve the performance of the knee MRI reconstruction. Meanwhile, higher SSIM results indicate better

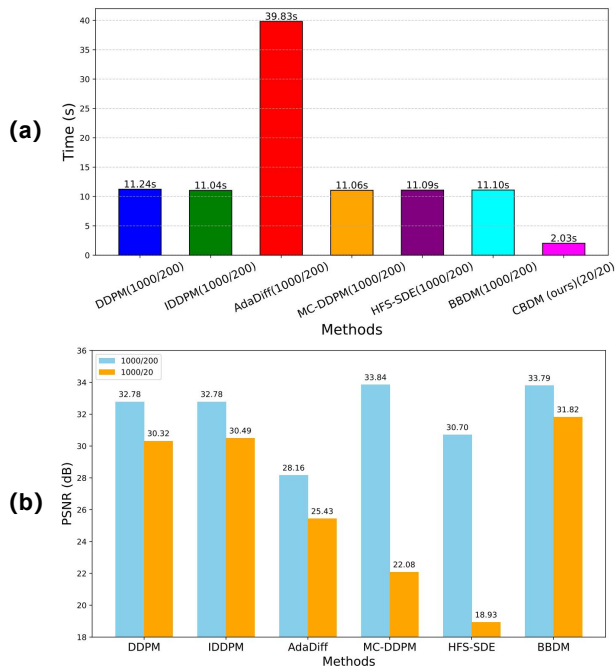


Figure 8: (a) A bar chart comparing the inference time of various diffusion methods. (b) A bar chart showing the changes in PSNR performance of other SOTA methods when their sampling steps are adjusted to match those of CBDM.

structural fidelity of the reconstruction results. Table 5 presents a comparative analysis of the settings for $t1$ and $t2$ during the training process of our CBDM. Similarly, Table 6 compares the effects of different settings for $\sqrt{\sigma_{t1}}$ and $\sqrt{\sigma_{t2}}$. The results reveal that the time steps and noise variances for the two bridge diffusion processes can vary in each step of the cyclical diffusion process, highlighting the versatility and adaptability of the CBDM training approach.

4.6. Limitations

Although the cycle-consistent design enhances the image representation, our training process still requires two bridge diffusion models for training at the same time, which may bring more training costs. Additionally, the performance in out-of-distribution experiments still drops as shown in Table 3. Therefore, future work will explore

diffusion models with lower training costs and stronger generalization capabilities.

5. Conclusion

We present a cyclical bridge diffusion model for accelerated MRI reconstruction. Specifically, a cycle consistency loss is used to help preserve fine-grained details and reduce the number of diffusion time steps for the image diffusion model training. Meanwhile, the Contourlet Decomposition Embedding Module extracts structural texture information in the frequency domain, capturing image structural texture and reducing artifacts. As a result, our CBDM approach effectively restores the normal human structure and texture details of MR images. Extensive experiments demonstrate that our method achieves state-of-the-art performance to transform under-sampled MRI data to fully-sampled MRI data on the benchmark fastMRI and IXI dataset.

References

- Aggarwal, H.K., Mani, M.P., Jacob, M., 2018. Modl: Model-based deep learning architecture for inverse problems. *IEEE Transactions on Medical Imaging* 38, 394–405.
- Bamberger, R.H., Smith, M.J., 1992. A filter bank for the directional decomposition of images: Theory and design. *IEEE Transactions on Signal Processing* 40, 882–893.
- Beck, A., Teboulle, M., 2009. A fast iterative shrinkage-thresholding algorithm for linear inverse problems. *SIAM Journal on Imaging Sciences* 2, 183–202.
- Burt, P.J., Adelson, E.H., 1987. The laplacian pyramid as a compact image code, in: *Readings in computer vision*. Elsevier, pp. 671–679.
- Cao, C., Cui, Z.X., Wang, Y., Liu, S., Chen, T., Zheng, H., Liang, D., Zhu, Y., 2024. High-frequency space diffusion model for accelerated mri. *IEEE Transactions on Medical Imaging* .
- Chen, Y., Firmin, D., Yang, G., 2021. Wavelet improved gan for mri reconstruction, in: *Medical Imaging 2021: Physics of Medical Imaging*, pp. 285–295.
- Cimpoi, M., Maji, S., Vedaldi, A., 2015. Deep filter banks for texture recognition and segmentation, in: *Proceedings of the IEEE/CVF Conference on Computer Vision and Pattern Recognition*, pp. 3828–3836.
- Cole, E.K., Pauly, J.M., Vasanawala, S.S., Ong, F., 2020. Unsupervised mri reconstruction with generative adversarial networks. *arXiv preprint arXiv:2008.13065* .
- Cui, Z.X., Cheng, J., Zhu, Q., Liu, Y., Jia, S., Zhao, K., Ke, Z., Huang, W., Wang, H., Zhu, Y., et al., 2021. Equilibrated zeroth-order unrolled deep networks for accelerated mri. *arXiv preprint arXiv:2112.09891* .
- Dar, S.U., Yurt, M., Karacan, L., Erdem, A., Erdem, E., Cukur, T., 2019. Image synthesis in multi-contrast mri with conditional generative adversarial networks. *IEEE Transactions on Medical Imaging* 38, 2375–2388.
- Fabian, Z., Heckel, R., Soltanolkotabi, M., 2021. Data augmentation for deep learning based accelerated mri reconstruction with limited data, in: *Proceedings of the International Conference on Machine Learning*, pp. 3057–3067.
- Goodfellow, I., Pouget-Abadie, J., Mirza, M., Xu, B., Warde-Farley, D., Ozair, S., Courville, A., Bengio, Y., 2014. Generative adversarial nets. *Advances in Neural Information Processing Systems* 27.
- Griswold, M.A., Jakob, P.M., Heidemann, R.M., Nittka, M., Jellus, V., Wang, J., Kiefer, B., Haase, A., 2002. Generalized autocalibrating partially parallel acquisitions (grappa). *Magnetic Resonance in Medicine* 47, 1202–1210.
- Güngör, A., Dar, S.U., Öztürk, Ş., Korkmaz, Y., Bedel, H.A., Elmas, G., Ozbey, M., Çukur, T., 2023. Adaptive diffusion priors for accelerated mri reconstruction. *Medical Image Analysis* , 102872.
- Ho, J., Jain, A., Abbeel, P., 2020. Denoising diffusion probabilistic models, in: *Advances in Neural Information Processing Systems*, pp. 6840–6851.
- Ho, J., Salimans, T., 2022. Classifier-free diffusion guidance. *arXiv preprint arXiv:2207.12598* .

- Hou, R., Li, F., 2022. Idpcnn: Iterative denoising and projecting cnn for mri reconstruction. *Journal of Computational and Applied Mathematics* 406, 113973.
- Hou, R., Li, F., Zeng, T., 2023. Fast and reliable score-based generative model for parallel mri. *IEEE Transactions on Neural Networks and Learning Systems* .
- Huo, Y., Xu, Z., Bao, S., Assad, A., Abramson, R.G., Landman, B.A., 2018. Adversarial synthesis learning enables segmentation without target modality ground truth, in: *Proceedings of the International Symposium on Biomedical Imaging*, pp. 1217–1220.
- Hyun, C.M., Kim, H.P., Lee, S.M., Lee, S., Seo, J.K., 2018. Deep learning for undersampled mri reconstruction. *Physics in Medicine & Biology* 63, 135007.
- Isola, P., Zhu, J.Y., Zhou, T., Efros, A.A., 2017. Image-to-image translation with conditional adversarial networks, in: *Proceedings of the IEEE/CVF Conference on Computer Vision and Pattern Recognition*, pp. 1125–1134.
- Jeelani, H., Martin, J., Vasquez, F., Salerno, M., Weller, D.S., 2018. Image quality affects deep learning reconstruction of mri, in: *Proceedings of the International Symposium on Biomedical Imaging*, pp. 357–360.
- Karras, T., Aittala, M., Aila, T., Laine, S., 2022. Elucidating the design space of diffusion-based generative models. *Advances in Neural Information Processing Systems* 35, 26565–26577.
- Knoll, F., Hammernik, K., Zhang, C., Moeller, S., Pock, T., Sodickson, D.K., Akcakaya, M., 2020. Deep-learning methods for parallel magnetic resonance imaging reconstruction: A survey of the current approaches, trends, and issues. *IEEE Signal Processing Magazine* 37, 128–140.
- Li, B., Xue, K., Liu, B., Lai, Y.K., 2023. Bbdm: Image-to-image translation with brownian bridge diffusion models, in: *Proceedings of the IEEE/CVF Conference on Computer Vision and Pattern Recognition*, pp. 1952–1961.
- Lu, C., Zhou, Y., Bao, F., Chen, J., Li, C., 2022. A fast ode solver for diffusion probabilistic model sampling in around 10 steps. *Advances in Neural Information Processing Systems* , 1–31.
- Lv, J., Wang, C., Yang, G., 2021. Pic-gan: a parallel imaging coupled generative adversarial network for accelerated multi-channel mri reconstruction. *Diagnostics* 11, 61.
- Nichol, A.Q., Dhariwal, P., 2021. Improved denoising diffusion probabilistic models, in: *Proceedings of the International Conference on Machine Learning*, pp. 8162–8171.
- Peng, C., Guo, P., Zhou, S.K., Patel, V.M., Chellappa, R., 2022. Towards performant and reliable undersampled mr reconstruction via diffusion model sampling, in: *Proceedings of the International Conference on Medical Image Computing and Computer-Assisted Intervention*, Springer. pp. 623–633.
- Pruessmann, K.P., Weiger, M., Scheidegger, M.B., Boesiger, P., 1999. Sense: sensitivity encoding for fast mri. *Magnetic Resonance in Medicine* 42, 952–962.
- Ronneberger, O., Fischer, P., Brox, T., 2015. U-net: Convolutional networks for biomedical image segmentation, in: *Proceedings of the International Conference on Medical Image Computing and Computer-Assisted Intervention*, Springer. pp. 234–241.
- Sartoretti, E., Sartoretti, T., Binkert, C., Najafi, A., Schwenk, Á., Hinnen, M., van Smoorenburg, L., Eichenberger, B., Sartoretti-Schefer, S., 2019. Reduction of procedure times in routine clinical practice with compressed sense magnetic resonance imaging technique. *PloS one* 14, e0214887.
- Shitrit, O., Riklin Raviv, T., 2017. Accelerated magnetic resonance imaging by adversarial neural network, in: *Deep Learning in Medical Image Analysis, DLMIA 2017*, Springer. pp. 30–38.
- Song, J., Meng, C., Ermon, S., 2020a. Denoising diffusion implicit models. *arXiv preprint arXiv:2010.02502* .
- Song, Y., Sohl-Dickstein, J., Kingma, D.P., Kumar, A., Ermon, S., Poole, B., 2020b. Score-based generative modeling through stochastic differential equations. *arXiv preprint arXiv:2011.13456* .

- Sriram, A., Zbontar, J., Murrell, T., Zitnick, C.L., De-fazio, A., Sodickson, D.K., 2020. Grappanet: Combining parallel imaging with deep learning for multi-coil mri reconstruction, in: Proceedings of the IEEE/CVF International Conference on Computer Vision.
- Sun, J., Li, H., Xu, Z., et al., 2016. Deep admm-net for compressive sensing mri. *Advances in Neural Information Processing Systems* 29.
- Wang, S., Su, Z., Ying, L., Peng, X., Zhu, S., Liang, F., Feng, D., Liang, D., 2016. Accelerating magnetic resonance imaging via deep learning, in: Proceedings of the International Symposium on Biomedical Imaging, pp. 514–517. doi:10.1109/ISBI.2016.7493320.
- Xie, Y., Li, Q., 2022. Measurement-conditioned denoising diffusion probabilistic model for under-sampled medical image reconstruction, in: Proceedings of the International Conference on Medical Image Computing and Computer-Assisted Intervention, Springer. pp. 655–664.
- Yang, A., Finkelstein, M., Koo, C., Doshi, A.H., 2024. Impact of deep learning image reconstruction methods on mri throughput. *Radiology: Artificial Intelligence* 6, e230181.
- Yang, G., Lv, J., Chen, Y., Huang, J., Zhu, J., 2021. Generative adversarial networks (gan) powered fast magnetic resonance imaging—mini review, comparison and perspectives. *arXiv preprint arXiv:2105.01800*.
- Zaitsev, M., Maclaren, J., Herbst, M., 2015. Motion artifacts in mri: A complex problem with many partial solutions. *Journal of Magnetic Resonance Imaging* 42, 887–901.
- Zhang, J., Ghanem, B., 2018a. Ista-net: Interpretable optimization-inspired deep network for image compressive sensing, in: Proceedings of the IEEE/CVF Conference on Computer Vision and Pattern Recognition, pp. 1828–1837.
- Zhang, J., Ghanem, B., 2018b. Ista-net: Interpretable optimization-inspired deep network for image compressive sensing, in: Proceedings of the IEEE/CVF Conference on Computer Vision and Pattern Recognition, pp. 1828–1837.
- Zhang, Q., Chen, Y., 2022. Fast sampling of diffusion models with exponential integrator. *arXiv preprint arXiv:2204.13902*.
- Zheng, H., Fang, F., Zhang, G., 2019. Cascaded dilated dense network with two-step data consistency for mri reconstruction. *Advances in Neural Information Processing Systems* 32.
- Zhou, L., Lou, A., Khanna, S., Ermon, S., 2023. Denoising diffusion bridge models.
- Zhu, J.Y., Park, T., Isola, P., Efros, A.A., 2017. Unpaired image-to-image translation using cycle-consistent adversarial networks, in: Proceedings of the IEEE/CVF International Conference on Computer Vision, pp. 2223–2232.